Non-thermal radio emission from colliding flows in classical nova V1723 Aql

Jennifer H. S. Weston,[1]★ J. L. Sokoloski,[1]★ Brian D. Metzger,[1] Yong Zheng,[1] Laura Chomiuk,[2] Miriam I. Krauss,[3] Justin D. Linford,[2] Thomas Nelson,[4] Amy J. Mioduszewski,[3] Michael P. Rupen,[5] Tom Finzell[2] and Koji Mukai[6,7]

[1]*Columbia Astrophysics Laboratory, Columbia University, New York, NY 10027, USA*
[2]*Department of Physics and Astronomy, Michigan State University, East Lansing, MI 48824, USA*
[3]*National Radio Astronomy Observatory, PO Box O, 1003 Lopezville Road, Socorro, NM 87801, USA*
[4]*School of Physics and Astronomy, University of Minnesota, 116 Church Street SE, Minneapolis, MN 55455, USA*
[5]*National Research Council of Canada, Herzberg Astronomy and Astrophysics Programs, Dominion Radio Astrophysical Observatory, PO Box 248, Penticton, BC V2A 6J9, Canada*
[6]*CRESST and X-ray Astrophysics Laboratory, NASA/GSFC, Greenbelt, MD 20771, USA*
[7]*Department of Physics, University of Maryland, Baltimore County, 1000 Hilltop Circle, Baltimore, MD 21250, USA*

ABSTRACT

The importance of shocks in nova explosions has been highlighted by *Fermi*'s discovery of γ-ray-producing novae. Over three years of multiband Very Large Array radio observations of the 2010 nova V1723 Aql show that shocks between fast and slow flows within the ejecta led to the acceleration of particles and the production of synchrotron radiation. Soon after the start of the eruption, shocks in the ejecta produced an unexpected radio flare, resulting in a multipeaked radio light curve. The emission eventually became consistent with an expanding thermal remnant with mass $2 \times 10^{-4}\,M_\odot$ and temperature 10^4 K. However, during the first two months, the $\gtrsim 10^6$ K brightness temperature at low frequencies was too high to be due to thermal emission from the small amount of X-ray-producing shock-heated gas. Radio imaging showed structures with velocities of 400 km s^{-1} (d/6 kpc) in the plane of the sky, perpendicular to a more elongated 1500 km s^{-1} (d/6 kpc) flow. The morpho-kinematic structure of the ejecta from V1723 Aql appears similar to nova V959 Mon, where collisions between a slow torus and a faster flow collimated the fast flow and gave rise to γ-ray-producing shocks. Optical spectroscopy and X-ray observations of V1723 Aql during the radio flare are consistent with this picture. Our observations support the idea that shocks in novae occur when a fast flow collides with a slow collimating torus. Such shocks could be responsible for hard X-ray emission, γ-ray production, and double-peaked radio light curves from some classical novae.

Key words: binaries: general – novae, cataclysmic variables – stars: variables: general – white dwarfs – stars: winds, outflows – radio continuum: stars.

1 INTRODUCTION

The most common type of stellar explosion, a nova occurs when accretion of material on to a white dwarf (WD) from its binary companion ignites a thermonuclear runaway, expelling matter and causing the system to brighten. Because novae occur frequently – an estimated 35 yr^{-1} in our Galaxy alone (Shafter 1997) – they can be used to probe stellar explosions, astrophysical outflows,

nuclear burning, and accretion. However, to find an accurate model of these eruptions, one must account for the presence of shocks, bipolar outflows, rings, clumping, and other asymmetries that have been shown to be present in different nova systems (e.g. Slavin, O'Brien & Dunlop 1995; Shara et al. 1997; Sokoloski, Rupen & Mioduszewski 2008; Chomiuk et al. 2014).

Radio observations of novae furnish a useful tool for recording the evolution of a nova's expanding shell and understanding the properties of the ejecta. In the radio, the ejecta remain optically thick to thermal emission at significantly lower densities than at shorter wavelengths. The ejecta can therefore typically be detected for months to years in the radio. In classical novae, radio emission

★E-mail: jennifer@astro.columbia.edu (JHSW); jeno@astro.columbia.edu (JLS)

is generally observed to be dominated by thermal bremsstrahlung radiation, interpreted as emanating from an expanding shell (Seaquist & Palimaka 1977; Hjellming 1979; Bode & Evans 2008).

While non-thermal emission has long been evident in nova systems with red-giant companions, such as RS Oph (Taylor et al. 1989), in classical novae with main-sequence companions, the dominant features in historical radio light curves and spectra are generally consistent with an expanding thermal shell producing free–free emission (Hjellming 1996, 1979; Seaquist et al. 1980; Bode & Evans 2008). Given some reasonable assumptions about the temperature and morphology of a thermal shell, comprehensive radio spectral coverage as the ejecta transition from being optically thick to optically thin enables observers to infer the density profile of the nova shell and estimate the total mass ejected. Resolved images in radio allow for further constraints on the morphology, temperature, and evolution of the thermal shell. However, only a handful of classical novae have been well observed at multiple radio frequencies from the optically thick rise to the optically thin decay, including HR Del (Hjellming 1979), V1500 Cyg (Seaquist et al. 1980), and V1974 Cyg (Hjellming 1996). This lack is particularly noticeable in the first few months immediately following the outburst, when the thermal radio emission is expected to be faint.

Technological improvements to the Karl G. Jansky Very Large Array (VLA) and other radio telescopes within the past five years have vastly increased the sensitivity of radio observations. Our group has been using the updated capabilities of the VLA in concert with optical and X-ray observations to create a more complete and multiwavelength picture of the mass-loss history of novae. V1723 Aql was the first classical nova to be discovered in outburst after the upgrade to that facility. Beginning two weeks after the initial discovery of the eruption of V1723 Aql in 2010 September, the observations of Krauss et al. (2011), in combination with the additional radio monitoring presented here, have produced one of the best, most detailed radio light curves of a classical nova to date.

Discovered in outburst at its optical maximum (mag 12.4) on 2010 September 11, and with a magnitude of fainter than 14.0 on 2010 September 10, we take that discovery of V1723 Aql as the start of the outburst, t_0 = MJD 55450.5 (Balam, Hsiao & Graham 2010; Yamanaka, Itoh & Komatsu 2010). Optical observations revealed V1723 Aql to be a typical 'fast nova' (Gaposchkin 1957) of the Fe II spectral type, fading by two magnitudes within 20 d (Yamanaka et al. 2010). Despite the lack of extensive optical or IR followup, the observations in the first few weeks of the eruption showed rapid reddening, implying the formation of dust particles as early as 20 d after the start of the outburst (Nagashima et al. 2013). Emission lines of Hα on the day of discovery had full width at zero intensity of 3000 km s^{-1}, implying a maximum expansion velocity v_{obs} = 1500 km s^{-1} (Yamanaka et al. 2010). The nova was neither embedded in the wind of an M-giant mass donor nor a recurrent nova – making it representative of the majority of novae (Nagashima et al. 2013).

Although V1723 Aql showed no unusual aspects in its early optical behaviour, the VLA observations revealed an unexpected radio flare peaking roughly 45 d after the start of the optical outburst (Krauss et al. 2011). Krauss et al. (2011) found that during this flare, the radio flux density rose as $t^{3.3}$, far more rapidly than the t^2 expected from freely expanding, isothermal, optically thick thermal ejecta. The radio spectrum during the flare was also inconsistent with that of an optically thick thermal source of a fixed temperature (Krauss et al. 2011). With only 175 d of radio monitoring, Krauss et al. (2011) were not able to conclusively determine the origin of this flare, or whether V1723 Aql would evolve according to the

more standard picture of radio emission from a classical nova after this unexpected activity. We label the observations between the start of the eruption and day 175, presented in Krauss et al. (2011), as the *early-time* observations, and the new observations presented here (between day 198 and day 1281) as the *late-time* observations.

We describe below how the combination of the *early-time* and *late-time* radio observations reveals that whereas the late-time observations are dominated by the expected thermal emission from a freely expanding nova shell, there is strong evidence that the early-time flare was dominated by non-thermal emission. In Section 2, we present our late-time observations and data reduction procedure; in Section 3, we describe the observational findings and data analysis; in Section 4, we introduce a thermal model for the remnant after day 200, explore the possibility of the early-time emission being produced by relativistic particles accelerated in internal shocks, and propose that the ejecta from V1723 Aql had a morpho-kinetic structure with internal shocks like that of γ-ray producing nova V959 Mon. In Section 5, we highlight our conclusions.

2 OBSERVATIONS AND DATA PROCESSING

Building on the work of Krauss et al. (2011), who used VLA observations during the first six months of the outburst of V1723 Aql to identify the bright early-time flare, we present our observations of V1723 Aql with the VLA between 2011 March (day 198) and 2014 March (day 1281) – from six months to three and a half years after the start of the eruption (see Table 1). For completeness, Table 1 additionally lists the early-time observations of Krauss et al. (2011). The late-time observations were taken using the VLA WIDAR correlator at a range of frequencies spanning 2.5–36.5 GHz with bandwidths of 2048 MHz, distributed in two tuneable 1048 MHz sidebands and using 8-bit samplers. The central frequencies in each band may have had some slight variation due to frequency-dependent flagging in post-processing to minimize radio frequency interference. At each frequency, on-source observations were alternated with observations of a nearby phase reference calibrator (J1851+0035, J1832−1035, or J1822−0938), with an additional observation of a standard flux calibration source (either 3c286 or 3c48). We used observations of the unpolarized calibrator J0319+4130 (3c84) for polarization leakage solutions. The late-time data presented here comprise 29.5 h of observations (14.9 h on source V1723 Aql) and 658 GB of raw data over three years and two full cycles of VLA configurations. Including the earlier programmes presented in Krauss et al. (2011), the data total 1604 GB and 59.5 h (28.2 h on source) between 2010 September 25 and 2014 March 15.

We processed all data using National Radio Astronomy Observatory (NRAO) Common Astronomy Software Applications (CASA) or Astronomical Image Processing System (AIPS). As is standard procedure, we obtained a bandpass solution and used it to solve for gain amplitude and phase, then applied these solutions to the source, using the 'Perley-Butler 2010' flux density scale. Imaging was completed using the CLEAN algorithm (Högbom 1974) with Briggs weighting, with the additional use of super-resolution techniques (Staveley-Smith et al. 1993) on day 1281 to resolve small structures during that observation. Radio flux densities were measured by fitting two dimensional Gaussians to the emitting region in the image plane with the task *imfit*. We estimated uncertainties in flux density by adding in quadrature the error from the Gaussian fit and systematic errors of 1 per cent at frequencies below 19 GHz and 3 per cent at those above, with the results presented in Table 2 and Figs 1 and 2. All error bars correspond to 1σ uncertainties.

Table 1. VLA observations of V1723 Aql, between 2010 September and 2014 March.

Observation date	MJD	Day[a]	Epoch	VLA program ID	Configuration	Observed bands	Time[b] (min)
Early time observations (previously presented in Krauss et al. 2011)							
2010 September 25	55464.1	13.6	0	10B-200	DnC	C, Ka	57
2010 October 3	55472.1	21.6	1	10B-200	DnC	C, Ka	21
2010 October 6	55475.1	24.6	2	10B-200	DnC/C	C, Ka	58
2010 October 15	55483.1	32.6	3	10B-200	C	C, Ka	48
2010 October 18	55487.1	36.6	4	10B-200	C	L, C, X	43
2010 October 19	55488.1	37.6	4	10B-200	C	C, Ka	28
2010 October 24	55493.1	42.6	5	10B-200	C	L, C, X	43
2010 October 29	55497.0	46.5	6	10B-200	C	L, C, X, Ka	71
2010 November 7	55507.8	57.2	7	10B-200	C	L, C, X, Ka	74
2010 December 3	55533.9	83.4	8	10B-200	C	L, C, X, Ka	84
2010 December 18	55548.9	98.4	9	10B-200	C	L, C, X	52
2010 December 21	55551.7	101.2	9	10B-200	C	C, Ka	34
2011 January 14	55575.8	125.3	10	10B-200	C	L,C,X, Ka	70
2011 January 30	55591.8	141.3	11	10B-200	CnB	L,C,X, Ka	63
2011 March 5	55625.5	175.0	12	11A-254	B	C, X, Ka	51
Late time observations							
2011 March 28	55648.6	198.1	13	11A-254	B	C, X, Ka	52
2011 August 2	55775.2	324.7	14	11A-254	A	C, X, Ku, K, Ka	116
2011 August 27	55800.2	349.7	15	11A-254	A	C, X, Ku, K, Ka	72
2011 November 11	55876.1	425.6	16	11B-170	D	C, X, Ku, K, Ka	58
2012 January 14	55940.8	490.3	17	11B-170	DnC	C, X, Ku, K, Ka	58
2012 April 19	56037.0	586.5	18	11B-170	C	C, X, Ku, K, Ka	58
2012 December 8	56269.0	818.5	19	12B-226	A	C, X, Ku, K	20
2012 December 22	56283.6	832.5	20	12B-226	A	X, Ka	45
2013 March 27	56378.4	927.9	21	13A-465	D	C, X, Ku, K, Ka	106
2013 August 30	56534.1	1083.6	22	13A-461	C	L, C, X, Ku, K, Ka	98
2013 November 30	56626.7	1176.5	23	13A-465	B	L, S, X, Ka	101
2014 March 15	56731.5	1281.0	24	13A-465	A	X, Ku	112

Notes. [a]Days after initial detection of outburst, 2010 September 11.

[b]Total time of observations on-source.

3 DATA ANALYSIS AND RESULTS

3.1 Flux density and spectral evolution

Around day 45, the flux densities reached a local maximum and subsequently declined at all frequencies, with another local maximum at all frequencies between days 200 and 400 (see Table 2 and Fig. 1). We refer to the radio brightening that peaked around day 45 as the *early-time flare*. There was an additional local maximum between these two bright peaks at the higher frequencies. The flux densities at the highest frequencies reached higher values than those at lower frequencies during both major peaks. For example, during the final local maxima (between days 200 and 400), the 36.5 GHz flux density peaked at 12.80 ± 0.39 mJy, whereas the 5.2 GHz flux density peaked at 1.14 ± 0.05 mJy. Moreover, the flux densities at *Ka* band (28.5/36.5 GHz) reached their highest values on day 198, whereas the flux densities at lower frequencies peaked later, with *C*-band flux densities (5.2/6.8 GHz) peaking on day 426 or 490.

During the late-time period, the radio spectrum evolved from one that rose with frequency to one that fell slightly with frequency (see Fig. 2 and Table 3). To obtain spectral indices and 1σ uncertainty estimates for those spectral indices for each observation ($S_\nu \propto \nu^\alpha$, where S_ν is the flux density at frequency ν, and α is the spectral index), we fit data with a power law using IDL's 'linfit' function, which minimizes the χ^2 statistic, with the data and error bars in log space. With the simple single power-law model, we found acceptable fits ($\chi_r^2 \lesssim 1.5$, where χ_r^2 is the reduced χ^2 value) only for days

198 and 818, between which time the spectral index fell from $\alpha = 1.47 \pm 0.05$ to $\alpha = -0.22 \pm 0.08$.

The late-time transition from a rising to a falling spectrum occurred via the appearances of first one, and then a second, spectral break. We refer to the three distinct portions of the spectrum when two breaks were present as the *low-frequency*, *transition*, and *high-frequency* parts of the spectrum. We refer to the corresponding spectral indices as α_{low}, α_{trans}, and α_h, and the frequencies at which the breaks between the regions of different spectral index occur as ν_{lt} (for the break between the low-frequency and transition part of the spectrum) and ν_{th} (for the break between the transition and high-frequency portion of the spectrum). For epochs where both a poor χ^2 fit and the residuals of the simple power-law model suggested a spectral break, we fit the data with broken power-law models with one or two breaks. Fig. 2 shows the spectra and fits, and Table 3 reports the power-law models that combined to minimize χ^2, with the break frequencies indicating where the power-law models intersect. The uncertainties for the break frequencies correspond to the range of frequencies at which the power laws intersected given a $\pm 1\sigma$ range for the spectral indices. We were able to find acceptable fits for a single break power-law model on day 325, and for a double-break power-law model on days 426 and 587.

Fig. 2 and Table 3 show the evolution of the spectrum and its component segments. The low-frequency spectral index α_{low} typically had values of approximately 1.4, α_{trans} typically had values between 0.2 and 0.6, and α_h typically had values of approximately -0.2. The spectrum on day 490 (see Fig. 2) shows the characteristic

Table 2. Flux densities for late-time observations of V1723 Aql.

Epoch	Day	Observed flux density (mJy)					
		2.5 GHz (*S* band)	3.3 GHz (*S* band)	5.2 GHz (*C* band)	6.8 GHz (*C* band)	8.7 GHz (*X* band)	9.5 GHz (*X* band)
13	198	. . . *	. . .	0.75 ± 0.02	. . .	1.53 ± 0.03	. . .
14	325	. . .	. . .	0.89 ± 0.03	1.32 ± 0.03	1.88 ± 0.03	. . .
15	250	. . .	. . .	0.91 ± 0.03	1.33 ± 0.03	1.97 ± 0.03	. . .
16	425	. . .	. . .	1.14 ± 0.05	1.59 ± 0.04	2.09 ± 0.04	. . .
17	490	. . .	. . .	1.10 ± 0.03	1.60 ± 0.05	1.79 ± 0.03	. . .
18	587	. . .	. . .	0.92 ± 0.02	1.30 ± 0.02	1.39 ± 0.03	. . .
19	818	. . .	. . .	0.70 ± 0.05	0.76 ± 0.06	. . .	. . .
21	928	. . .	. . .	1.09 ± 0.10	0.61 ± 0.03	0.77 ± 0.04	0.71 ± 0.02
22	1084	. . .	. . .	0.43 ± 0.02	0.48 ± 0.02	0.44 ± 0.02	0.45 ± 0.02
23	1177	0.42 ± 0.04	0.25 ± 0.02	. . .	. . .	0.41 ± 0.05	0.34 ± 0.01
		12.9 GHz (*Ku* band)	16.1 GHz (*Ku* band)	20.1 GHz (*K* band)	25.6 GHz (*K* band)	28.5 GHz (*Ka* band)	36.5 GHz (*Ka* band)
13	198	. . .	. . .	5.48 ± 0.17	7.76 ± 0.23	9.02 ± 0.28	12.81 ± 0.39
14	325	3.20 ± 0.12	3.94 ± 0.10	4.87 ± 0.16	5.35 ± 0.17	5.84 ± 0.18	6.76 ± 0.22
15	350	2.98 ± 0.05	3.59 ± 0.05	4.20 ± 0.13	4.30 ± 0.14	4.43 ± 0.14	5.38 ± 0.20
16	426	2.42 ± 0.03	2.71 ± 0.08	3.03 ± 0.10	3.03 ± 0.10	2.87 ± 0.09	3.12 ± 0.11
17	490	2.10 ± 0.03	2.07 ± 0.03	. . .	. . .	2.42 ± 0.09	2.05 ± 0.10
18	587	1.53 ± 0.04	. . .	1.87 ± 0.08	1.72 ± 0.07	1.85 ± 0.08	1.69 ± 0.10
19	818	0.66 ± 0.06	0.56 ± 0.05	. . .	0.43 ± 0.09	. . .	. . .
20	832	. . .	. . .	. . .	. . .	0.71 ± 0.13	0.62 ± 0.19
21	928	0.53 ± 0.02	0.59 ± 0.02	0.54 ± 0.03	0.56 ± 0.03	0.55 ± 0.02	0.54 ± 0.03[c]
22	1084	0.43 ± 0.03	0.42 ± 0.02	0.51 ± 0.08	0.32 ± 0.03	0.38 ± 0.05	0.35 ± 0.04[c]
23	1177	. . .	. . .	. . .	. . .	0.23 ± 0.02	0.19 ± 0.02[c]
24	1281	0.27 ± 0.01[a]	0.26 ± 0.02[b]	. . .	. . .	. . .	. . .

Notes. * '. . .' indicates no observation at this frequency on this day.
[a] Values are reported for 13.5 GHz.
[b] Values are reported for 14.5 GHz.
[c] Values are reported for 32.5 GHz.

low-frequency, transition, and high-frequency spectral regions most clearly. On day 198, the spectrum was well described by a simple power law with a low-frequency type spectral index. On day 325, the lowest frequencies maintained a steep rising spectrum of $\alpha_{low} = 1.44 \pm 0.05$; above 16.1 GHz, the spectrum became shallower, with $\alpha_{trans} = 0.64 \pm 0.05$. The spectra continued to show this break between α_{low} and α_{trans} in observations between days 325 and 587, during which time ν_{lt} decreased from 13.6 GHz to 6.7 GHz. Observations between days 426 and 587 showed the additional break at higher frequencies, ν_{th}, above which the spectrum flattened to $\alpha_h = 0.13 \pm 0.13$ on day 426, $\alpha_h = -0.64 \pm 0.23$ on day 490, and $\alpha_h = -0.08 \pm 0.19$ on day 587. While the very small uncertainties in our flux densities reveal some deviation from a single power law during the last five observations, the spectrum was nevertheless approximately described by a fairly flat single power law during that time.

3.2 Resolved images

V1723 Aql was resolved at the highest observed radio frequency on day 832 (*Ka*-band) and on day 1281 (*Ku*-band) (see Fig. 3, panel a). The remnant was therefore large enough to be spatially resolved, with the difference between the integrated and the peak flux density greater than five times the root mean square error (rms). Fig. 3 shows images from the second and third of the three observations during which the VLA was in A configuration (which gives the highest spatial resolution). The image from day 832 (2012 December 22) at 32.4 GHz shows that the radio emitting material was elongated in the NW/SE direction and had visible substructure. The full width at half-maximum (FWHM) of the brightness profile along the major axis of the fitted Gaussian was 160 ± 10 mas, with the FWHM

along the minor axis of 110 ± 20 mas. The position angle (PA) of the major axis was 160° ± 10° (where PA is the east of north). The clean beam size was 90 mas × 60 mas, and the peak flux density was 130 ± 20 μJy beam^{-1}, with an rms of 22.6 μJy beam^{-1}. To more accurately estimate the size scale of the source, we fit the brightness profile, deconvolved from the synthesized clean beam, to a Gaussian. Taking the width of the Gaussian along the major axis at a flux density of twice the rms as an indicator of size, the size scale along the major axis on day 832 was 250 ± 10 mas. The substructure showed two resolved components with brightness peaks separated by 70 mas. They were aligned perpendicular to the major axis of the elongated material, with a PA of about 80°.

Taking into account the expected expansion by 50 per cent between day 832 and day 1281, the size of the radio-emitting remnant on day 1281 indicates that the material that was most extended on day 832 had faded, and only the denser inner structure remained detectable. By day 1281 (2014 March 14; using robust =0.5 in the CLEAN algorithm), the resolved material was elongated in the NE/SW direction, instead of the NW/SE elongation seen on day 832. The fitted Gaussian had an FWHM of 180 ± 10 mas along the major axis (which had a PA of 35° ± 5°), and an FWHM along the minor axis of 133 ± 7 mas. The peak flux density was 118.5 ± 3.5 μJy beam^{-1}, with rms of 3.32 μJy beam^{-1}, resulting in a size scale of 408 ± 2 mas. With a clean beam size of 160 mas × 130 mas, no substructure was resolved. If we consider the two components visible on day 832, and extrapolate from their 70 mas separation, we would have expected a separation of 108 mas on day 1281 – which was not within the formal resolution limits of this observation. Therefore, we additionally used super-resolution techniques (Staveley-Smith et al. 1993) to examine the more detailed structure of the source on this day, deconvolving the source with the slightly
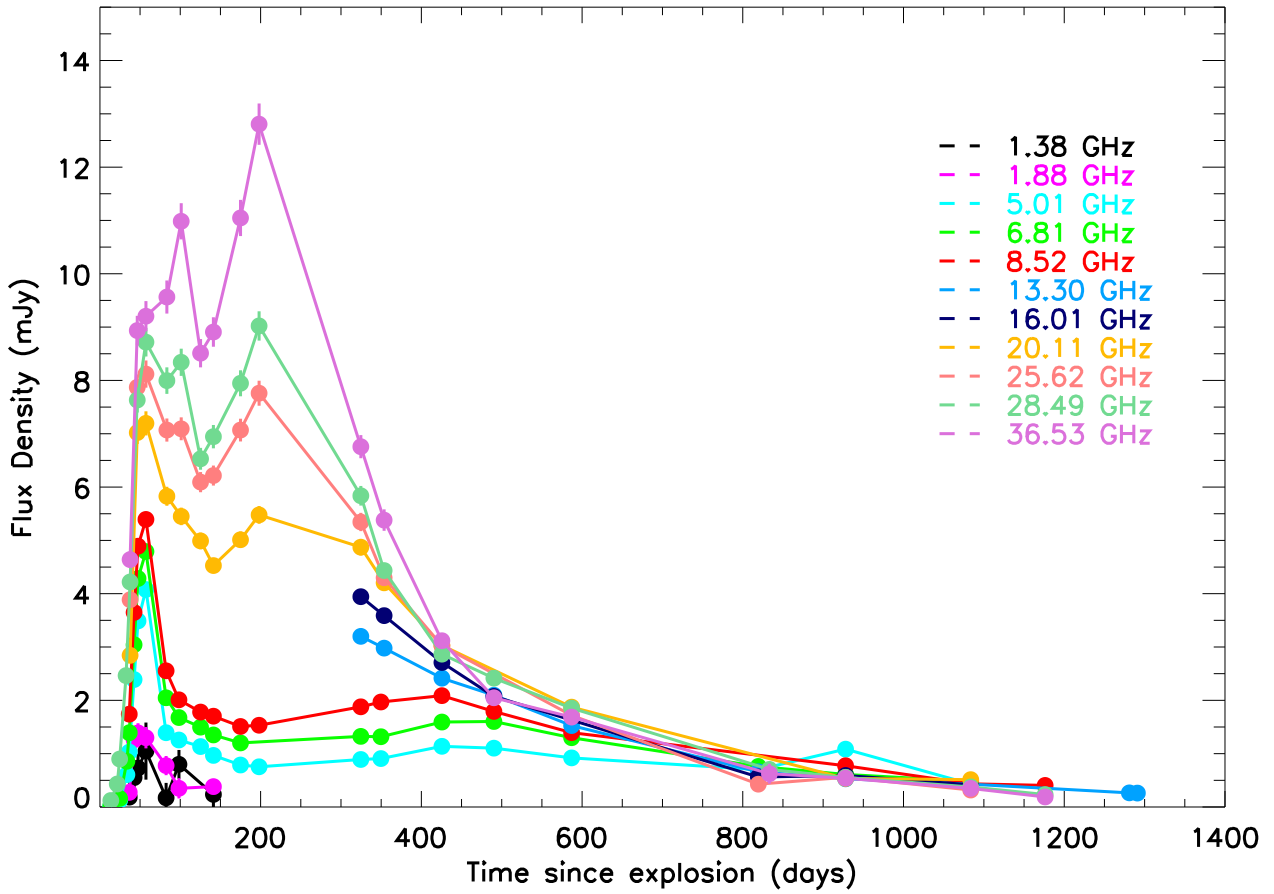
Figure 1. Observed flux densities of V1723 Aql between 2010 September and 2014 March. Error bars are as reported in Table 2, but may be too small to be visible.

smaller beam size of 90 × 90 mas. Using this technique, we uncovered a ring-like structure with dimensions ∼0.22 × 1.5 arcsec and PA 45° (see Fig. 3, panel b), with an rms of 7.0 µJy beam^{-1}.

4 DISCUSSION

We propose that the radio emission from V1723 Aql – when considered in the context of published optical and X-ray observations – is most consistent with a picture in which the nova initially generated a slow outflow and then a faster flow. We argue below that the slow flow had a speed of a few hundred km s^{-1}, and that it was likely concentrated towards the equatorial plane of the binary. The faster flow had a maximum speed of at least 1500 km s^{-1}, and it collided with the early, slow ejecta within a few weeks of the start of the eruption, producing the early-time flare. The collisions led to shocks that heated some of the ejecta to temperatures above 10^7 K, and also accelerated particles to relativistic speeds. The slow-moving material probably collimated the faster flow into a biconical structure. Fig. 4 shows a cartoon of this toy model. The scenario that we propose for V1723 Aql is consistent with the one that Chomiuk et al. (2014) suggested for the γ-ray producing nova V959 Mon.

In the discussion below, we present evidence that supports the picture of a fast flow that collided with, and was shaped by, a preceding slow outflow. To diagnose the flows without the complexity of non-thermal emission from the early-time shock, we begin in Section 4.1 by describing how the brightness temperature and radio

spectral evolution at late times were consistent with a freely expanding thermal plasma with a temperature of around 10^4 K. The density profile and radio images of this radio-emitting plasma suggest that it had a roughly bipolar or biconical outer structure, and a shell-like inner structure with a likely equatorial density enhancement. In Section 4.2, we show that the early-time radio flare was probably dominated by synchrotron emission. Given the low X-ray flux during the flare (Krauss et al. 2011) and high brightness temperatures, it cannot be attributed to thermal emission alone. In Section 4.3, we discuss how V1723 Aql relates to other classical novae in its behaviour and shape, including those that produce γ-rays.

4.1 Origin of the late-time radio emission: expanding thermal shell

4.1.1 General physical constraints

We obtained a first estimate of the distance to V1723 Aql by using our maximum extension of the remnant on day 832, when our image had the highest spatial resolution (smallest clean beam). Since by day 832, some of the outermost material had become optically thin and therefore the remnant might not have a sharp outer edge, we took the maximum size scale to be the extent along the major axis of the Gaussian fit, down to a flux density of twice the rms. When we compare the size scale of 251 ± 7 mas with the expectation for ejecta expanding with a maximum velocity of $v_{obs} = 1500$ km s^{-1} (Yamanaka et al. 2010), we obtain a distance of 5.7 ± 0.4 kpc, or ∼6 kpc. The assumption that the maximum expansion speed in the
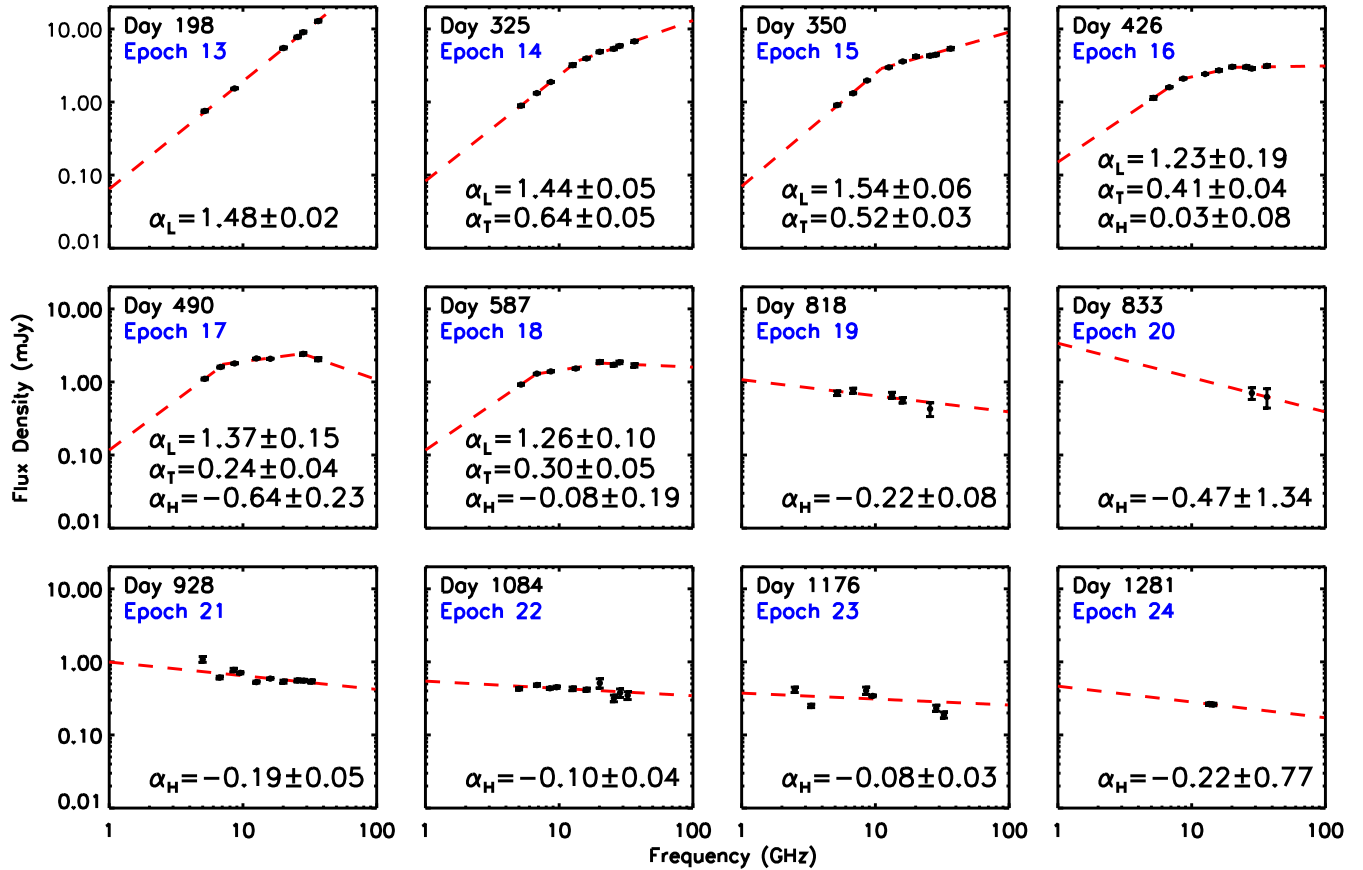
Figure 2. Spectra of V1723 Aql between 2011 March and 2014 March, with lines showing the best-fitting spectral indices α (where $S_\nu \propto \nu^\alpha$). For epochs where the spectral index appears to be a function of frequency, spectral indices are listed from lowest frequency range to highest. See Table 3.

Table 3. Spectral indices. For days where we fit models with spectral breaks, ν_{lt} refers to the break between the low-frequency and transition parts of the spectrum, and ν_{th} refers to the break between the transition and high-frequency portions of the spectrum. α_{low}, α_{trans}, and α_h are the corresponding spectral indices for these segments. β shows the density profile $n \propto 1/r^\beta$ associated with the spectral index α for a spherical shell transitioning between optically thick and optically thin thermal emission (Wright & Barlow 1975), and χ_r^2 and df are the reduced chi-square statistic and the number of degrees of freedom, respectively.

Epoch	Day	Model*	α_{low}	α_{trans}	α_h	ν_{lt} (GHz)	ν_{th} (GHz)	χ_r^2	df	β
13	198	SPL	1.48 ± 0.02					0.73	4	
14	325	BPL	1.44 ± 0.05	0.64 ± 0.05		13.6		0.45	7	2.04 ± 0.06
15	350	BPL	1.54 ± 0.06	0.52 ± 0.03		11.3		2.75	7	1.92 ± 0.03
16	426	DBPL	1.23 ± 0.19	0.41 ± 0.04	0.03 ± 0.08	8.3	21.2	0.60	7	1.84 ± 0.03
17	490	DBPL	1.37 ± 0.15	0.24 ± 0.04	-0.64 ± 0.23	7.3	27.8	2.53	5	1.69 ± 0.03
18	587	DBPL	1.26 ± 0.10	0.30 ± 0.05	-0.08 ± 0.19	6.7	21.2	1.00	6	1.74 ± 0.04
19	818	SPL			-0.22 ± 0.08			1.26	3	
20	832	SPL			-0.47 ± 1.34			–	0	
21	928	SPL			-0.19 ± 0.02			8.40	8	
22	1084	SPL			-0.10 ± 0.04			2.12	8	
23	1177	SPL			-0.08 ± 0.03			24.19	4	
24	1281	SPL			-0.22 ± 0.77			–	0	

Notes. *SPL – single power-law fit.
BPL – broken power-law fit (one break).
DBPL – double broken power-law fit (two breaks).

plane of the sky is equal to the maximum radial velocity is valid if the remnant is approximately spherical or, for a bipolar flow, has wide opening angles (as is suggested by the $1/r^2$ density profile, see below).

Other methods of distance determination using optical data are either not possible or extremely unreliable. There are two means

of nova distance determination using optical data. The most commonly utilized method is the Maximum Magnitude Rate of Decline (MMRD) method (Della Valle & Livio 1995); the other method involves utilizing high-resolution spectra to identify absorption lines from intervening interstellar clouds of known distance (e.g. Chomiuk et al. 2012). No high-resolution spectra of V1723 Aql
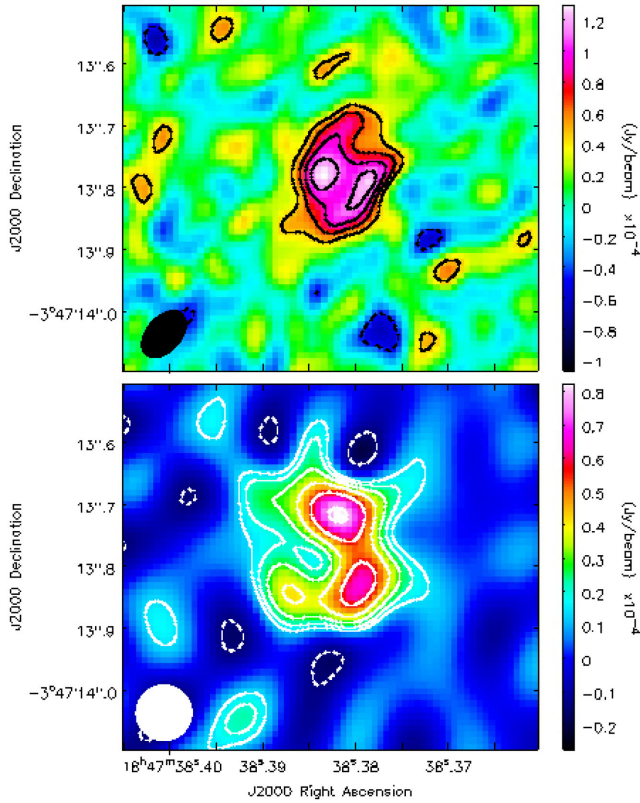
Figure 3. Top panel: spatially resolved image of V1723 Aql taken on 2012 December 22 in *Ka*-band (32.4 GHz). When fitted to a two-dimensional Gaussian, the brightness profile has an FWHM along the major axis of 160 ± 10 mas and along the minor axis of 110 ± 20 mas, where the major axis has a position angle of 160° ± 10° east of north. Contour levels are at [−2, 2, 3, 4, 5] × rms with rms = 2.26×10^{-5} Jy. There are two resolved components roughly perpendicular to the major axis of the Gaussian profile, with a separation of 70 mas at an angle of 82° E of N. Bottom panel: spatially resolved image of V1723 Aql taken on 2014 March 14 in *Ku*-band (14 GHz). When deconvolved with a beam size of 90 mas × 90 mas, we see a ring-like structure. Contour levels are at [−2, 2, $2\sqrt{2}$, 4, $4\sqrt{2}$, 8, $8\sqrt{2}$, 16, $16\sqrt{2}$, 32] ×rms with rms = 7.01×10^{-6} Jy.

were available, making it impossible for us to use the latter method. The MMRD technique has been the subject of serious critiques in recent publications (e.g. Kasliwal et al. 2011; Cao et al. 2012). Further, the episode of dust formation observed in V1723 Aql confounds the determination of t_2, rendering the already dubious MMRD method useless for distance determination.

Using $d \sim 6$ kpc, we find that the brightness temperature after day 200 was consistent with the late-time radio emission emanating from a thermal remnant with $T \sim 10^4$ K, where T is the electron temperature. Brightness temperature is

$$T_{\rm b}(\nu, t) \sim \frac{S_\nu(t) c^2 D^2}{2\pi k_b \nu^2 (v_{\rm obs} t)^2}, \qquad (1)$$

where c is the speed of light, k_b is Boltzmann's constant, t is the time since eruption, and $v_{\rm obs}$ is the observed maximum radial velocity (e.g. Bode & Evans 2008). Using our values from day 200, for example, we find that $T_{\rm b} = 1.5 \pm 0.4 \times 10^4$ K at 5.2 GHz, which is consistent with $\sim 10^4$ K. Ionized ejecta from novae are typically found to have electron temperatures of around 10^4 K, which is also approximately the equilibrium temperature for photoionized plasma that is cooled by forbidden line emission (Seaquist &
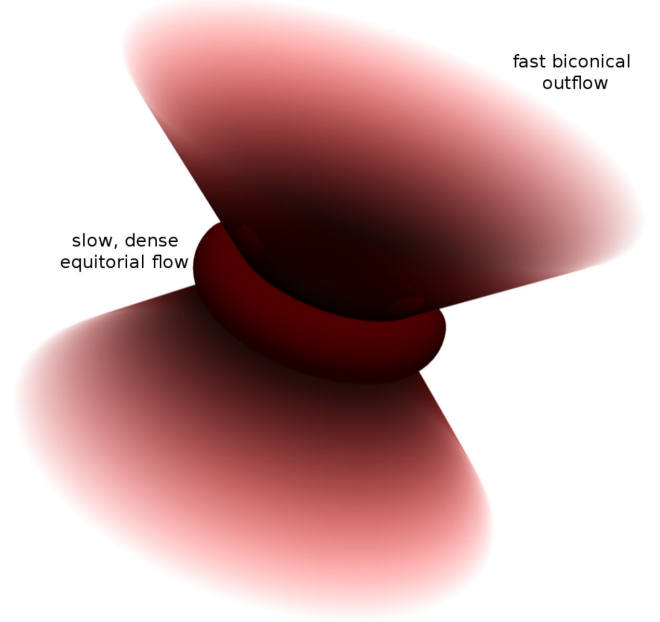

Figure 4. We propose a picture where a fast, bipolar outflow is shaped by a slow moving equatorial torus. Shocks arose in the collision region between the slow and fast flows.

Palimaka 1977; Taylor et al. 1987; Bode & Evans 2008). This $\sim 10^4$ K ejecta temperature can be sustained by photoionization heating by the WD for up to a year after the nova eruption (Cunningham, Wolf & Bildsten 2015). A brightness temperature around this value therefore provides support for thermal bremsstrahlung as the dominant emission mechanism at late times in V1723 Aql.

Moreover, the detailed evolution of the radio spectrum between days 198 and 350 (approximately 6 to 12 months after the start of the outburst) places constraints on the density profile in the outermost regions of the expanding ejecta. We consider the point at which the free–free optical depth at a given frequency (τ_ν) is unity, where the emitting material transitions from optically thick to optically thin. The high spectral index of $\alpha_{\rm low} \approx 1.5$ on day 198 indicates that at that time, the ejecta were dense enough to be optically thick for frequencies of up to at least 36.5 GHz. Therefore, these $\tau_\nu = 1$ surfaces were very close to the outer boundary of the ejecta for all frequencies at which we observed on day 198. The appearance of the first spectral break on day 325, however, reveals that by that time, the density of the ejecta had dropped enough that at least part of the ejecta were beginning to become optically thin for frequencies above $\nu_{\rm lt}$. Thus, the radii of the $\tau_\nu = 1$ surfaces at frequencies above $\nu_{\rm lt}$ were no longer increasing as fast as that of the ejecta. The spectral index above the first spectral break ($\alpha_{\rm trans}$) is directly related to the density profile in these transitioning ejecta. For an isothermal shell with a density profile of the form $n(r) \propto 1/r^\beta$ (where n is density and r is distance from the central binary), the spectral index is given by $\alpha_{\rm trans} \sim \frac{4\beta - 6.2}{2\beta - 1}$ for $\beta \geq 1.5$ (Wright & Barlow 1975). For a measured $\alpha_{\rm trans}$, we thus have $\beta = \frac{31 - 5\alpha_{\rm trans}}{20 - 10\alpha_{\rm trans}}$ (see Table 3). Our measurement of $\alpha_{\rm trans} \approx 0.6$ on days 325 and 350, when only the outermost portions of the ejecta were beginning to become optically thin, suggests that the density profile in the outermost part of the ejecta was proportional to $1/r^2$.

The appearance of a second break in the spectrum on day 426, roughly 14 months after the start of the eruption, shows that the ejecta had become optically thin at frequencies above $\nu_{\rm th}$. Optically

thin thermal emission has a spectral index of $\alpha = -0.1$ (e.g. Bode & Evans 2008),as we approximately found above $\nu_{\rm th}$. Between the two breaks at $\nu_{\rm lt}$ and $\nu_{\rm th}$, the spectral index of the transitioning region $\alpha_{\rm trans}$ provides information about the density profile deeper within the ejecta. With a value of approximately 0.3 on days 490 and 587, when these two breaks are clear, $\alpha_{\rm trans}$ suggests an average density profile deep within the remnant of roughly $1/r^{1.7}$ – somewhat flatter than in the outermost regions of the remnant.

The observed evolution of $\alpha_{\rm trans}$ is unlikely to be due to a temperature gradient. Although a temperature gradient can in principle affect the spectral index, the effect drops out for a $1/r^2$ density profile (Cassinelli & Hartmann 1977; Barlow 1979). Moreover, a radial decrease in the ionized gas fraction would also only serve to increase the steepness of the spectrum during the transition period (Wright & Barlow 1975), in contrast to what we observed. Therefore, the observed flattening of the $\alpha_{\rm trans}$ in the interior of the ejecta is unlikely to have been due to a temperature or ionization gradient.

For a more promising avenue to explain the declining $\alpha_{\rm trans}$, Wright & Barlow (1975) note that non-spherical geometries can cause the total number density of the gas to fall off less rapidly than $n \propto r^{-2}$ for a constant, finite duration flow. For example, a disc geometry would fall off as $n \propto r^{-1}$ and in a cylindrical geometry n would be independent of r (Wright & Barlow 1975). Therefore, that for V1723 Aql $\alpha_{\rm trans}$ appears to flatten slightly with time may indicate that the inner remnant is more confined towards the equatorial plane than the outer remnant – as in the case of the biconical flow collimated by a dense, slow torus in V959 Mon (Chomiuk et al. 2014). If this is the case, a bi-polar outflow could result in an overestimate of mass by up to a factor of 2 (Ribeiro et al. 2014). Nevertheless, since the density profile of $1/r^2$ in the outer regions of the ejecta suggest that any bipolar flow must have a wide opening angle, we can nevertheless use a spherical model to obtain reasonable estimates of the ejecta parameters.

The flux density near $\nu_{\rm th}$ furnishes a rough estimate of the inner radius of the ejecta on the dates when this break frequency was observable. The ejecta are optically thin, with optical depth $\tau_\nu < 1$, at frequencies above $\nu_{\rm th}$. They are optically thick, with $\tau_\nu > 1$ at frequencies below $\nu_{\rm th}$. Integrating the absorption coefficient for radio emission at $\nu_{\rm th}$ along the line of sight through the ejected envelope therefore gives exactly $\tau_\nu = 1$, suggesting that the photosphere lies near the inner edge of the ejected shell for $\nu_{\rm th}$. At the frequency $\nu_{\rm th}$, the rough angular size of the photosphere is

$$\frac{\theta}{\text{arcsec}} = \left(\frac{S_\nu}{\text{mJy}}\right)^{1/2} \left(\frac{T_{\rm b}}{1200\ \text{K}}\right)^{-1/2} \left(\frac{\nu_{\rm th}}{\text{GHz}}\right)^{-1}, \qquad (2)$$

(Rybicki & Lightman 1979), where θ is the full angular diameter of the photosphere. Using the break frequencies $\nu_{\rm th}$ and flux densities at these frequencies from days 426, 490, and 587 (see Fig. 2), and taking $T_{\rm b} \approx 10^4$ K, we find that the inner edge of the ejecta had an approximate radius of between 10 and 15 mas during these observations, which corresponds to an expansion speed $v_{\rm i}$ of the slowest, innermost ejecta of between 200 and 400 km s^{-1} $(d/6{\rm kpc})(T_{\rm b}/10^4\ \text{K})$, $^{-1/2}$, assuming all the ejecta were homologous and ejected at t_0.

Although these estimates do not provide any evidence that the inner radius increased between days 426 and 587, the estimates are uncertain enough that they do not place meaningful constraints on the actual evolution of the inner radius. The estimates do, however, indicate that the radio-emitting ejecta were geometrically thick (given that the outermost material moved away from the central binary at approximately 1500 km s^{-1}), though not uniquely or unusually so (e.g. Seaquist & Palimaka 1977).

The radio spectra during the second year of the eruption also enable us to make an estimate of the ejecta mass. We can obtain the emission measure of the ejecta at the $\tau_\nu = 1$ radio photosphere at $\nu_{\rm th}$ from the expression

$$\tau_\nu = 8.235 \times 10^{-2} \left(\frac{T}{\text{K}}\right)^{-1.35} \left(\frac{\nu}{\text{GHz}}\right)^{-2.1} \left(\frac{EM_{\rm rad}}{\text{cm}^{-6}\ \text{pc}}\right), \qquad (3)$$

where τ_ν is the free–free optical depth at frequency ν and $EM_{\rm rad} = \int_{R_{\rm i}}^{R_{\rm o}} n^2(r)\, {\rm d}r$ is the emission measure integrated from the inner radius $R_{\rm i}$ to the outer radius $R_{\rm o}$ (Lang 1980). With the emission measure, inner and outer radii, and density profile in hand for the observation with the clearest break frequency $\nu_{\rm th}$, we can estimate the mass of the ejecta. For the purpose of this mass estimate, we take a spherically symmetric shell and density proportional to $1/r^2$, as estimated from $\alpha_{\rm trans}$ in the outer regions of the ejecta. Using the inner radius on day 426 from above, which gives the velocity of the inner edge as $v_{\rm i} = 360$ km s^{-1} and outer radius assuming a maximum expansion velocity of 1500 km s^{-1}, we find an approximate ejecta mass of $1.6(\pm0.2) \times 10^{-4}$ M$_\odot$, which is of the same order of magnitude as is typically found in nova ejecta mass estimates (Bode & Evans 2008). Repeating this process for other days on which multiple breaks were visible results in similar mass estimates – on day 490, we find a mass of $1.6(\pm0.2) \times 10^{-4}$ M$_\odot$, and on day 587 we find a mass of $1.7(\pm0.7) \times 10^{-4}$ M$_\odot$ (see Table 4).

4.1.2 The Hubble flow model

The gross properties of the radio-emitting ejecta at late times (after day 200) were consistent with expectations from the so-called Hubble flow model (Seaquist & Palimaka 1977; Hjellming 1979). In this model, a spherically symmetric shell is ejected from the WD instantaneously, but with a range of velocities, so that the velocity is proportional to the distance from the WD. A $1/r^2$ density profile, as we inferred from $\alpha_{\rm trans}$, corresponds to the mass being distributed uniformly over the velocities. Such a model has been applied to many historical novae, including V1974 Cyg (Hjellming 1996), V1500 Cyg (Seaquist et al. 1980), QU Vul (Taylor et al. 1988), and V723 Cas (Heywood et al. 2005). Given the brightness temperature after day 200 of near 10^4 K, and the evolution of the radio spectrum from initially rising with frequency (as expected for an optically thick shell) to falling slightly with frequency (as expected for an optically thin shell) via the appearance of two distinct spectral breaks, we conclude that it is reasonable to use a Hubble flow model to parametrize the ejecta that produced the late-time radio emission from V1723 Aql.

Table 4. Total ejecta mass M and minimum velocity ($v_{\rm i}$) as determined using the spectral breaks visible on days 426, 490, and 587. Mass estimates vary based on the density profile assumed.

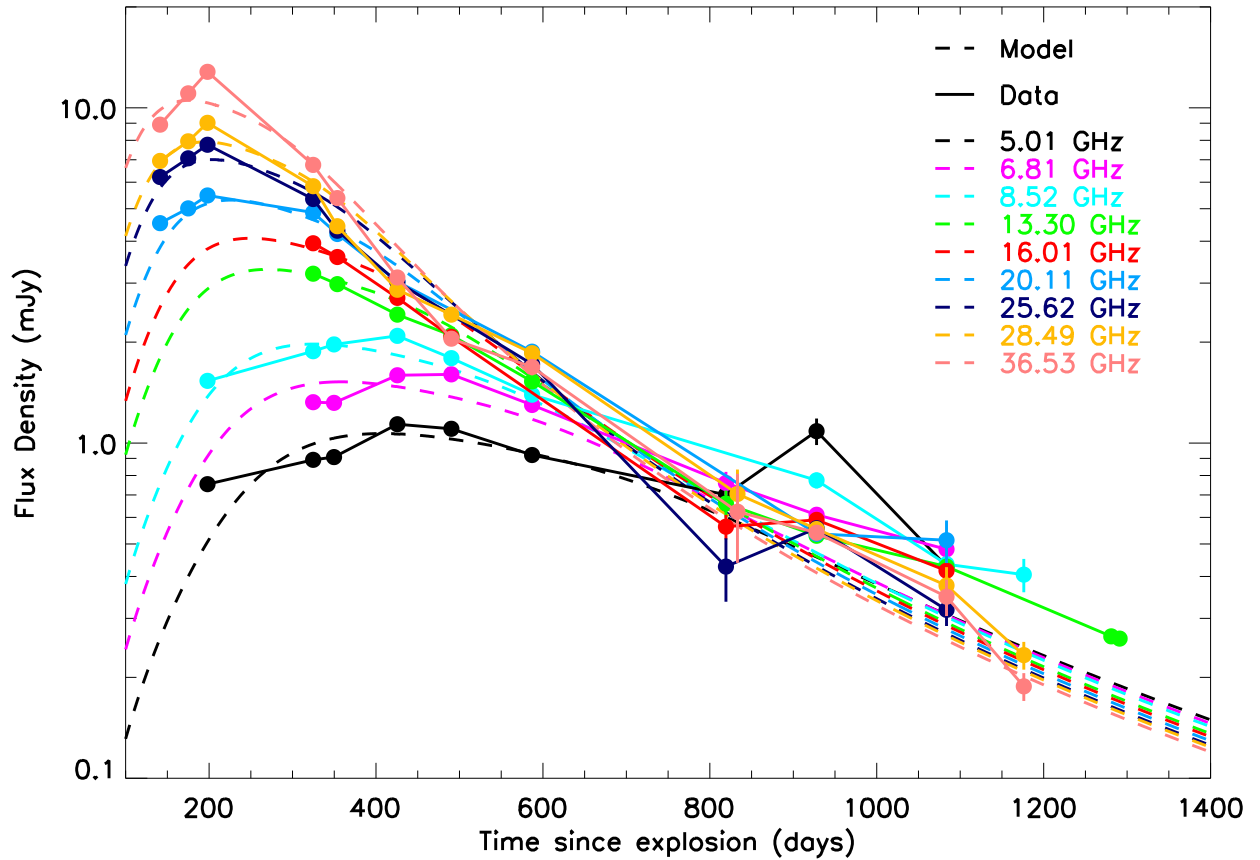| Epoch	Day	v_i (km s^{-1})	$\zeta = v_{\rm i}/v_{\rm obs}$	M (M$_\odot$), $n \propto 1/r^1$	M (M$_\odot$), $n \propto 1/r^2$	M (M$_\odot$), $n \propto 1/r^3$
16	426	360 ± 20	0.24 ± 0.01	$2.7 \pm 0.3 \times 10^{-4}$	$1.6 \pm 0.2 \times 10^{-4}$	$0.9 \pm 0.2 \times 10^{-4}$
17	490	210 ± 10	0.14 ± 0.01	$4.0 \pm 0.4 \times 10^{-4}$	$1.6 \pm 0.2 \times 10^{-4}$	$0.6 \pm 0.1 \times 10^{-4}$
18	587	190 ± 20	0.13 ± 0.01	$4.6 \pm 1.6 \times 10^{-4}$	$1.7 \pm 0.7 \times 10^{-4}$	$0.7 \pm 0.3 \times 10^{-4}$

Figure 5. The late-time observations of V1723 Aql between 2011 March and 2014 March, presented here for the first time, with eight previously published data points from days 2011 January 31 and 2011 March 5 used to constrain the high-frequency light curves. Model indicates light curve of an expanding spherical thermal shell with a density profile of $1/r^2$, mass M = 1.7×10^{-4} M$_\odot$, ejecta temperature of T = 1.1×10^4 K, maximum velocity of v_{obs} = 1500 km s^{-1} distance of d = 6.0 kpc, and ratio of minimum to maximum velocity $\zeta = v_i/v_{obs} = 0.17$.

Although the Hubble flow model does not give a formally acceptable fit to the late-time radio emission, it is roughly consistent with the most dominant features in the data. Fig. 5 shows the Hubble flow model light curves that provide the best fit to the late-time radio data (where we have added eight data points published in Krauss et al. 2011 from days 141 and 175 to our measurements to help constrain the turnover of the high-frequency light curves). Taking the nova to have a distance of 6 kpc and using the expansion velocity measured by Yamanaka et al. (2010) on the day of discovery as the maximum velocity v_{obs} = 1500 km s^{-1}, ejected at t = 0, and allowing other parameters to vary, our best-fitting model has an ejecta mass of $M = 1.7 \times 10^{-4}$ M$_\odot$, a temperature of $T = 1.1 \times 10^4$ K, and a ratio of minimum to maximum velocity $\zeta = v_i/v_{obs} = 0.17$ (see Fig. 5). Given that the ejecta are clearly not spherically symmetric (see Fig. 3), and that the evolution of the spectral index α_{trans} from 0.6 to 0.3 suggests a flattening of the density profile over time, it is not too surprising that the Hubble flow model does not provide a formally acceptable fit. Overall, however, the fitting of the late-time radio data with a Hubble flow model indicates that if the ejecta were approximately spherical, then roughly 2×10^{-4} M$_\odot$ was ejected at a temperature of 10^4 K.

Comparing model light curves for a range of ejecta masses, temperatures, and shell thicknesses provides a measure of the uncertainty on these parameters. Fig. 6 suggests that the best-fitting parameters are accurate to within at least a factor of 2. In terms of the effect that modifying these parameters has on the model light curves, changing the distance would have influenced the maximum

flux density at each frequency, to which it is inversely related. Increasing the temperature of the shell increases the resulting flux density at all times, and causes the turnover from optically thick to thin to occur earlier. Increasing the maximum velocity also causes this transition to occur at earlier times. The ratio of the minimum and maximum velocity, ζ, relates to the flux density and the decline of the light curve after peak – a higher ratio corresponds to a geometrically thinner remnant, which both raises the maximum flux density and causes a swifter decline in flux density after this peak. Increasing the total ejecta mass in the model also causes an increase in flux density at all times, and causes a slower, later transition from optically thick to optically thin emission at all frequencies.

While our observations are generally consistent with a $n \propto r^{-2}$ density profile, we can additionally demonstrate the sensitivity of the total ejecta mass to the distribution of mass within the nova shell. For example, if we again use the observed spectral breaks to estimate the inner and outer radii of the shell and calculate the emission measure, we can estimate the mass of the shell with different density profiles. For example, by using the spectral breaks on day 587, we estimate an ejecta mass of $M \sim 4.6 \times 10^{-4}$ M$_\odot$ and $M \sim 0.7 \times 10^{-4}$ M$_\odot$ for densities profiles of $1/r$ and $1/r^3$, respectively (see Table 4). If the ejecta from V1723 Aql were clumpy rather than smooth, the total ejecta mass would be reduced. Clumping increases the flux density of an isothermal shell by up to a factor of $f^{-2/3}$, where f is the volume filling factor (Abbott, Bieging & Churchwell 1981). However, clumping would not influence the spectral index, nor the overall shape of the radio light
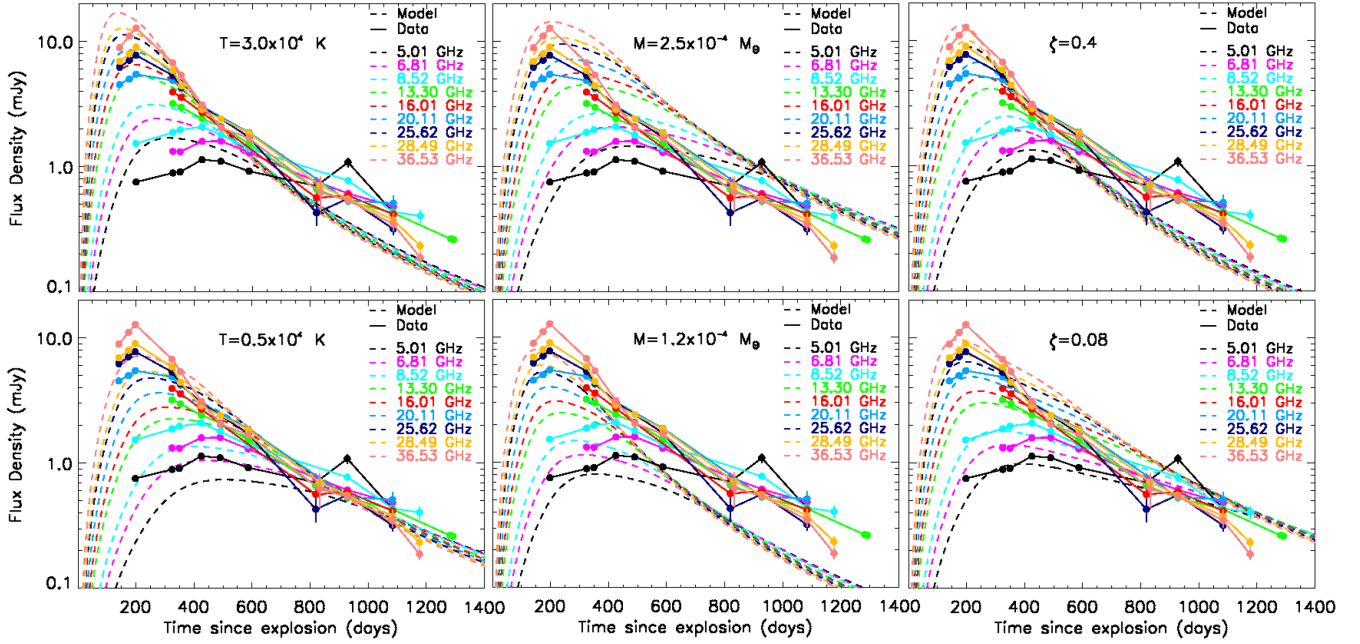
Figure 6. Variations of the Hubble flow model compared to the observed flux densities. Unless otherwise stated, the parameters for the model show distance of 6 kpc, maximum velocity of 1500 km s^{-1}, temperature of 1.1×10^4 K, mass of 1.7×10^{-4} M$_\odot$, and $\zeta = 0.17$. The leftmost column shows variation in temperature, with the top panel showing a temperature of 3×10^4 K and the bottom showing a temperature of 5×10^3 K. The middle column shows variation in mass: the top panel shows a model with mass 2.5×10^{-4} M$_\odot$, and the bottom panel shows 1.2×10^{-4} M$_\odot$. The right-hand column shows variation in shell thickness, varying the ratio of minimum to maximum velocity ζ. The top panel shows a ratio of 0.4, and the bottom shows a ratio of 0.08.

curve, as uniformly distributed clumping would affect the free–free flux similarly at all frequencies (Abbott et al. 1981; Leitherer & Robert 1991; Nelson et al. 2014).

4.2 Origin of the early time flare: particles accelerated in shocks within the ejecta

4.2.1 Brightness temperature of the ejecta

Whereas the late-time emission is consistent with originating in a thermal remnant with $T \sim 10^4$ K and a strong resemblance to a Hubble flow, the early-time emission is not (see Fig. 7). In fact, the $T \sim 10^4$ K ejecta were only revealed once the early-time flare faded. The brightness temperature at early times was strongly dependent on both frequency and time, with a maximum T_b of between $\sim 6 \times 10^4$ K at 36.5 GHz and $\sim 4 \times 10^6$ K at 1.4 GHz. Brightness temperature is an expression of surface brightness and represents a lower limit on the physical temperature of any thermally emitting material; for the flare to have been thermal, it would therefore have had to have been emitted by plasma with $T \geq 4 \times 10^6$ K.

During the early-time flare, however, the X-ray flux was too low for the radio flare to have been due to hot (X-ray emitting) plasma. For the radio flare to have been entirely thermal, it would have had to have been produced by plasma that was optically thick at 1.9 GHz, had an electron temperature $T \approx 4 \times 10^6$ K, and had a size scale of 3×10^{-4} pc$\left(\frac{v_{\rm obs}}{1500 \text{ km s}^{-1}}\right)\left(\frac{t}{43\,\rm d}\right)$. The flare could in principal also have been produced by free–free emission from hotter plasma that subtended a smaller solid angle on the sky. Krauss et al. (2011) detected X-ray emission from plasma with $T > 2 \times 10^7$ K on day 41 after the start of the eruption. For ejecta with $T = 2 \times 10^7$ K to be optically thick, the free–free optical depth would have to have

been greater than one:

$$\tau_{\rm ff} = 3.0 \times 10^{-12} \left(\frac{T}{2 \times 10^7 \text{ K}}\right)^{-1.35} \left(\frac{\nu}{1.9 \text{ GHz}}\right)^{-2.1} EM_{\rm rad} > 1. \tag{4}$$

This requirement corresponds to

$$\int n_e^2 \mathrm{d}l > 3.3 \times 10^{11} \left(\frac{T}{2 \times 10^7 \text{ K}}\right)^{1.35} \left(\frac{\nu}{1.9 \text{ GHz}}\right)^{2.1} \text{pc cm}^{-6}. \tag{5}$$

A hot plasma with a temperature five times the maximum T_b could in principal have produced the radio flare if it was optically thick at 1.9 GHz and subtended a solid angle that was 20 per cent that of the entire ejecta. A uniform-density spherical shell of that size, with shell thickness ℓ, would therefore require an electron density of

$$n_e > 6 \times 10^7 \times \left(\frac{T}{2 \times 10^7 \text{ K}}\right)^{0.675} \left(\frac{\nu}{1.9 \text{ GHz}}\right)^{1.05}$$

$$\times \left(\frac{\ell}{2.5 \times 10^{14} \text{ cm}}\right)^{-1/2} \text{cm}^{-3} \tag{6}$$

to be optically thick. Such hot plasma would produce an X-ray emission measure, $EM_x \equiv \int n_e^2 \mathrm{d}V$ (where V is the emitting volume), of approximately 8×10^{59} cm^{-3} (independent of ℓ), and (unless the shell was extremely thin) have a mass of a few times 10^{-6} M$_\odot$. On day 41, however, *Swift*/XRT detected X-rays with an EM_x of just $\sim 10^{56}$ cm^{-3}, indicating that there was not enough 2×10^7 K plasma to produce the observed radio flare. Even generating a model of the expected X-ray emission and assuming the highest reasonable absorbing column allowed by the X-ray spectral fit (3×10^{23} cm^{-2}), the observed X-ray flux was still an order of magnitude lower than would be required to explain the radio flare with thermal emission.
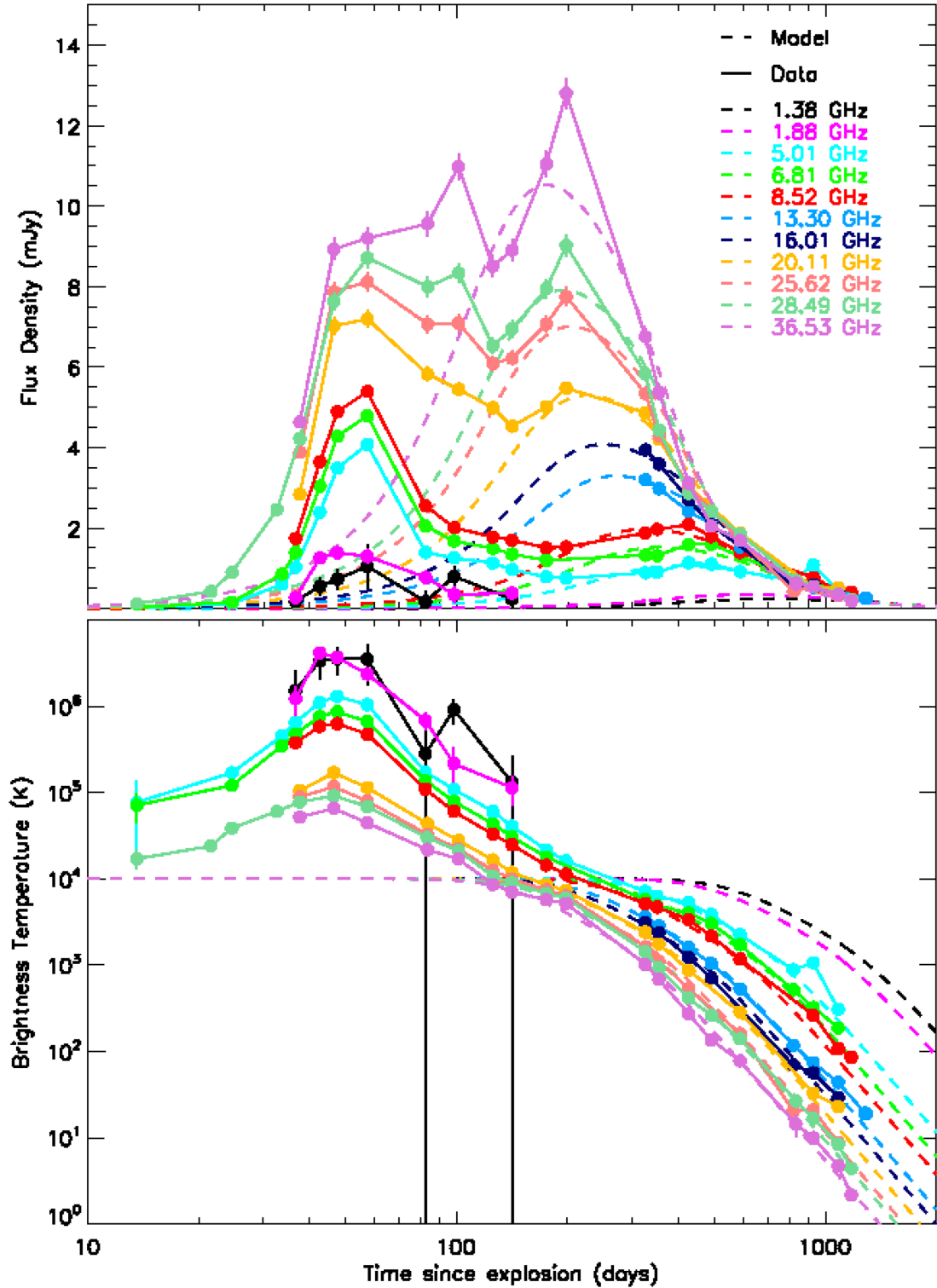
Figure 7. Flux densities (top panel) and brightness temperatures (bottom panel) for V1723 Aql between 2010 September and 2014 March. The dashed lines indicate the expected thermal emission from an expanding spherical shell with a density profile proportional to $1/r^2$, mass $M = 1.7 \times 10^{-4}\,\mathrm{M_\odot}$, ejecta temperature of $T = 1.1 \times 10^4$ K, maximum velocity of $v_{obs} = 1500$ km s^{-1}, distance of $d = 6.0$ kpc, and ratio of minimum to maximum velocity $\zeta = v_i/v_{obs} = 0.17$. The brightness temperature, which is an expression of surface brightness, is highly frequency dependent and peaks during the early-time flare at all frequencies. The great difference between the brightness temperatures during the early-time flare and the late-time peak highlights the physically distinct nature of the early and late radio brightenings.

The natural alternative to thermal emission is radio synchrotron emission from electrons accelerated in a shock.

The inconsistency between the radio flux density at 1.9 GHz and thermal radio emission expected from the 2×10^7 K X-ray-emitting plasma is independent of the distance to V1723 Aql. If we were to allow the temperature of the hot plasma to drop below 2×10^7 K (despite the constraints from Krauss et al. 2011), then the evidence for synchrotron emission would in principle depend on the distance to V1723 Aql. However, for the distance to be small enough to explain the radio flare with thermal emission, the outflow velocities become inconsistent with constraints from optical spectroscopy. Therefore, the combination of radio, X-ray, and optical observations appear to support a synchrotron emission mechanism.

4.2.2 Failure of thermal shock emission model

To further assess whether the early-time radio flare in V1723 Aql was thermal or non-thermal (synchrotron) in origin, we consider a one-dimensional, spherically symmetric model for internal shocks in novae, as presented in Metzger et al. (2014, hereafter M14). Consider a fast outflow of velocity $v_f \gtrsim 10^3$ km s^{-1} that collides with a slower shell of velocity $v_s \lesssim v_f$. For simplicity, assume that the mass of the slow shell is comparable to or lower than that of the fast material and is emitted at time $t = 0$. The fast outflow is emitted a time Δt after the slow shell, resulting in a collision radius

$$R_c \approx \frac{v_s v_f \Delta t}{v_f - v_s} \sim 6 \times 10^{13} \, v_{f,8} \frac{v_s}{\Delta v} \left(\frac{\Delta t}{\text{week}} \right) \text{ cm} \quad (7)$$

and time

$$t_c \approx \frac{R_c}{v_s} \approx \frac{v_f}{\Delta v} \Delta t, \quad (8)$$

where $\Delta v \equiv v_f - v_s$ and $v_{f,8} = v_f/10^8$ cm s^{-1}.

The predicted radio flare following this collision would be powered by the forward shock that emerges from the slow shell at approximately the time of the collision, i.e. $t_c \sim 50$ d. If both shells are ejected over a time-scale less than the duration of the peak optical activity, i.e. $\Delta t = (\Delta v/v_f)t_c \lesssim 2$ weeks, then the relative velocity between the shells must be relatively low, $\Delta v \lesssim v_f(\Delta t/t_{pk}) \approx 0.3v_f$, corresponding to a collision radius $R_c \sim v_s t_c \lesssim v_f t_c \sim 10^{15}$ cm for $v_f \sim 2 \times 10^3$ km s^{-1}.

The forward shock heats gas to a temperature (M14, equation 31),

$$T \approx 1.4 \times 10^7 \left(\frac{\Delta v}{10^3 \text{ km s}^{-1}} \right)^2 \text{ K} \approx 1.3 \times 10^6 \left(\frac{\Delta v}{0.3 v_f} \right)^2 v_{f,8}^2 \text{ K} \quad (9)$$

corresponding to an X-ray energy of $kT \sim 0.5$ keV for characteristic values $\Delta v \sim 0.3 v_f$ and $v_f \sim 2 \times 10^3$ km s^{-1}. For purposes of an estimate, here we have assumed that the slow shell is of comparable or lower density than the fast outflow.

For $n \approx 10^7$ cm^{-3} and $kT \approx 0.5$ keV, the cooling time of the gas is approximately one week for solar abundances, and even less for $X_Z \sim 0.1$ as assumed below. This suggests that the shock is likely to be radiative, in which case the resulting X-ray luminosity is given by

$$L_X \approx \frac{9\pi}{32} n m_p R_c^2 (\Delta v)^3$$

$$\approx 4 \times 10^{34} \left(\frac{n}{10^6 \text{ cm}} \right) \left(\frac{R_c}{10^{15} \text{ cm}} \right)^2 \left(\frac{\Delta v}{0.3 v_f} \right)^3 v_{f,8}^3 \text{ erg s}^{-1}, \quad (10)$$

where n is the (unshocked) density of the slow shell at the time of the collision. That the observed X-ray luminosity of $L_X \sim 3 \times 10^{32}$ erg s^{-1} near the radio peak (Krauss et al. 2011) is several orders of magnitude smaller than the fiducial value in equation (10) would require strong absorption of these soft X-rays by neutral gas ahead of the shock. Indeed, the bound-free X-ray optical depth ahead of the shock (M14, their equation 50)

$$\tau_X \approx 1.2 \left(\frac{X_Z}{0.1} \right) \left(\frac{n}{10^7 \text{ cm}^{-3}} \right) \left(\frac{R_c}{4 \times 10^{14} \text{ cm}} \right) \quad (11)$$

exceeds unity for $n \gtrsim 10^7$ cm^{-3}, where $X_Z = 0.1$ is the assumed mass fraction of CNO elements. This density corresponding to a minimum mass of the slow shell of $M_{sh} \gtrsim 4\pi(R_c^2 \Delta) n m_{ap} \sim 10^{-4}$ M$_\odot$ for $R_c \sim 10^{15}$ cm. For values of n below which $\tau_x < 1$, L_X in equation (10) still exceeds the observed X-ray luminosity by at least an order of magnitude; this may suggest that $v_{f,8} \lesssim 1$, or that a fraction of the shock power instead emerges at UV/soft X-ray energies below the *Swift* bandpass.

The maximum radio brightness temperature of radiative shocks at frequency ν is given by (M14, equation 65),

$$T_{b,\nu}^{max} \approx$$

$$\begin{cases} 3 \times 10^5 \ln \left[\frac{T}{T_{0,\nu}} \right] \text{ K} \underset{T \sim 10^6 - 10^7 \text{ K}}{\sim} 10^6 \text{ K} & n \gtrsim n_{th} \\ T_{0,\nu} = 10^5 \, v_{10}^{-2} \, n_7 \left(\frac{\Delta v}{v_f} \right) v_{f,8} \text{ K} \approx 4 \times 10^5 \, v_{10}^{-2} \left(\frac{n}{n_{th}} \right) \text{ K } n \lesssim n_{th}, \end{cases} \quad (12)$$

where $\nu_{10} = \nu/10$ GHz, $n_7 = n/10^7$ cm^{-3} and

$$n_{th} \approx 4 \times 10^7 \left(\frac{\Delta v}{0.3 v_f} \right)^{-1} v_{f,8}^{-1} \, v_{10}^2 \text{ cm}^{-3} \quad (13)$$

defines the pre-shock density above which the layer of X-ray ionized gas ahead of the shock is optically thick to free–free absorption, where a temperature of 2×10^4 K is assumed for the pre-shock gas. This value, appropriate to the photoionized layer slightly ahead of the shock (Metzger et al. 2014), may be slightly higher than the values expected for the bulk of the ejecta later, which our Hubble flow modelling finds is closer to 1×10^4 K.

The observed peak brightness temperature of V1723 Aql (see Fig. 7) exceeds the range given by equation (12) by more than order of magnitude, strongly suggesting a non-thermal origin for most of the observed radio emission. Furthermore, equation (12) was derived under the assumption that free–free emission is the sole source of cooling behind the shock. If the effects of line cooling are included, equation (12) greatly overestimates the brightness temperature, further enhancing the tension with thermal emission models.

It is difficult to produce a thermal model that fits the early-time radio data and is also consistent with the X-ray and late radio constraint. In Fig. 8, we applied the M14 model to the early light curve, modelling the shock as the collision of a fast wind with $v_f = 2100$ km s^{-1} and mass 0.8×10^{-4} M$_\odot$ and a shell with $v_s = 1300$ km s^{-1} with mass $M_{sh} = 1 \times 10^{-4}$ M$_\odot$. We assumed that the shells were released around $t = 0$, with a characteristic duration of the wind of 12 d, motivated by the observed optical decline rate. These parameters result in a post-shock velocity of $v_{obs} = 1500$ km s^{-1} and a total ejecta mass of $M \sim 1.8 \times 10^{-4}$ M$_\odot$, consistent with our late-time thermal model. Taking $n \propto 1/r^2$ and distance of 6 kpc, we were unable to reproduce the high-radio flux densities over the course of the shocks. We conclude that synchrotron
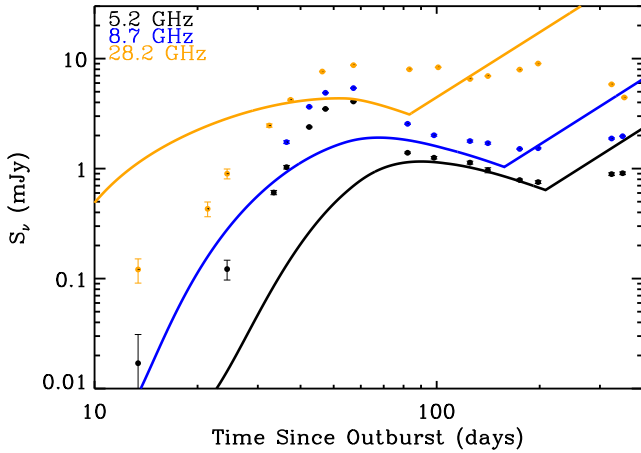
Figure 8. Observed flux densities and model flux densities in radio for a thermal shock. Assuming a distance of 6 kpc, the model uses a fast wind with an initial velocity $v_f = 2100\,\mathrm{km\,s^{-1}}$, mass $M_w = 0.8 \times 10^{-4}\,M_\odot$, and a characteristic duration of 12 d. The wind collides with a slower moving circumbinary shell with initial velocity $v_s = 1300\,\mathrm{km\,s^{-1}}$ and mass $M_s = 1 \times 10^{-4}\,M_\odot$. This results in a post shock velocity of $v_{obs} = 1500\,\mathrm{km\,s^{-1}}$ and total nova ejecta mass as $= 1.8 \times 10^{-4}\,M_\odot$, consistent with our late-time thermal model.

emission must therefore have at least partially powered the early-time flare.

4.2.3 Synchrotron emission from particles accelerated in shocks

The failure of thermal emission to account for the early-time radio flare suggests that the flare was dominated by synchrotron emission from particles that were accelerated in shocks. For one thing, shocks are common in classical novae. Evidence for shocks is provided by X-ray emission from plasma with temperature above 10^7 K (e.g. Mukai, Orio & della Valle 2008). Such temperatures arise naturally behind shock with speeds on the order of 1000 km s^{-1} (see equation 9). Furthermore, the recent identification of classical novae as a new class of γ-ray sources shows that not only are shocks ubiquitous in novae, but that relativistic particles are as well (Ackermann et al. 2014; Metzger et al. 2015a). A natural acceleration mechanism for these particles is *Fermi* acceleration in the shocks. In fact, radio observations have illustrated the existence of radio synchrotron emission in a normal nova – in *Fermi*-detected nova V959 Mon, Chomiuk et al. (2014) identified the location of γ-ray producing relativistic electrons as the region where a fast outflow collided with, and was shaped by, a dense equatorial torus. Although V959 Mon did not produce a strong early-time radio flare, its early-time radio emission was consistent with being synchrotron (Chomiuk et al. 2014). Whereas existing observations do not constrain the inclination of V1723 Aql, V959 Mon is viewed very nearly edge on (Chomiuk et al. 2014) – it is thus possible that some early non-thermal emission may have been obscured by the optically thick equatorial torus. Moreover, while the early-time flare in V1723 Aql suggests stronger non-thermal radio emission than that seen from V959 Mon, VLA observations of γ-ray-producing nova V1324 Sco (Nova Sco 2012) revealed a double peaked radio light curve similar to that of V1723 Aql (Finzell et al., in preparation).

Moreover, synchrotron emission is physically plausible for V1723 Aql. We expect the magnetic field behind the shock

to be amplified to a characteristic value (e.g. Caprioli & Spitkovsky 2014)

$$B = (6\pi\epsilon_B m_p n \Delta v^2)^{1/2}$$

$$\approx 0.05\epsilon_{B,-2}^{1/2}\left(\frac{n}{10^7\,\mathrm{cm}^{-3}}\right)^{1/2}\left(\frac{\Delta v}{0.3v_f}\right)v_{f,8}\,\mathrm{G}, \quad (14)$$

where $\epsilon_B = 10^{-2}\epsilon_{B,-2}$ is the fraction of the post-shock thermal energy placed into turbulent magnetic fields. The characteristic synchrotron frequency from an electron of Lorentz factor γ_e is given by

$$\nu_m \sim \frac{eB\gamma_e^2}{2\pi m_e c}$$

$$\sim 1.4\ \epsilon_{B,-2}^{1/2}\left(\frac{n}{10^7\,\mathrm{cm}^{-3}}\right)^{1/2}\left(\frac{\Delta v}{0.3v_f}\right)v_{f,8}\left(\frac{\gamma_e}{100}\right)^2\,\mathrm{GHz.} \quad (15)$$

For typical densities in the radio-producing nova shocks, $n \sim 10^7\,\mathrm{cm}^{-3}$, the production of radio synchrotron thus requires relativistic electrons with γ_e, corresponding to energies of a few hundred MeV. Such electrons may be directly accelerated at the shock (leptonic scenarios; see e.g. Kato 2015; Park, Caprioli & Spitkovsky 2015), or they may be created as electron/positron pairs produced by the decay of charged pions (hadronic scenarios). The Larmor radii of the radio emitting particles (γ_e of a few hundred) is extremely small compared to the size of the shock, so particles can easily remain within the acceleration region. As a comparison, supernovae remnants, which typically have post-shock densities on the order of $0.1-10\,\mathrm{cm}^{-3}$ and velocities of a few thousand km s^{-1} (e.g. Williams et al. 2014; Metzger et al. 2015b), using equation (14) would have magnetic field strengths scaling roughly as 50 µG, not atypical for post-shock remnants (as in e.g. Ressler et al. 2014). More detailed modelling of the non-thermal radio emission in novae (Vlasov et al., in preparation) find acceptable fits to the peak brightness temperature for assumed microphysical shock parameters ($\epsilon_e \sim 10^{-3}-10^{-2}, \epsilon_B \sim 10^{-2}$) as inferred from modelling supernova remnants (e.g. Morlino & Caprioli 2012).

The properties of the radio flare are also consistent with a synchrotron contribution. The expected time-scale for the decay of any synchrotron contribution is set by the size scale of the remnant divided by the expansion speed (Taylor et al. 1989), which for V1723 Aql is around 40 d, as observed. Krauss et al. (2011) did not detect linear polarization at 5.5 GHz on day 48, with a 3σ upper limit of 39 µJy (or 1 per cent). Similarly, on day 57, we detected no linear or circular polarization averaging across 1 GHz of bandwidth centred at 28.2 GHz, with 3σ upper limits of 0.42 mJy (9 per cent) for circular polarization and 0.63 mJy (6 per cent) for linear polarization. Given that the magnetic field geometry was likely to have been complex, the lack of strong polarization is not a concern for the synchrotron picture. That the radio spectrum rose with frequency during the radio flare indicates that the synchrotron emission was either self-absorbed or suffered from free–free absorption. Since synchrotron self-absorption would require the synchrotron-emitting region to have been extremely compact (i.e. have had a solid angle multiple orders of magnitude smaller than that of the remnant), whereas a reasonable amount of 10^4 K ionized gas could have led to observable absorption, we find free–free absorption more likely.

4.3 Nova shocks in the context of bipolar flows and γ-rays

The perpendicular structures evident in Fig. 3 are reminiscent of the perpendicular flows that Chomiuk et al. (2014) found to be

responsible for the generation of shocks and γ-rays in nova V959 Mon. In V959 Mon, radio observations showed that strong internal shocks produced synchrotron emission coincident with the γ-ray detection (Chomiuk et al. 2014). Radio images of the ejecta showed rapidly expanding bipolar flows, which faded over the course of 16 months to reveal an inner structure that collimated the outer flow (see Chomiuk et al. 2014, fig. 2d). Our image from day 1281 (see Fig. 3, panel b) reveals a similar inner structure that may be a shell with an equatorial density enhancement. The evolution of the radio spectrum of V1723 Aql may also indicate that the inner portions of its ejecta had a flatter density profile than the outer regions, as one might expect if an inner structure was more confined to the orbital plane (as in V959 Mon). Furthermore, the resolved image on day 832 showed two distinct components aligned roughly perpendicular to the axis of greatest elongation, which could be indicative of a limb-brightened collimating torus.

By associating V1723 Aql's multiple, distinct radio structures with different velocities, we identified flows that likely collided and led to shocks and particle acceleration. While optical spectra revealed the presence of a fast flow with maximum radial velocity $v_{obs} = 1500\,\mathrm{km\,s^{-1}}$ (Yamanaka et al. 2010), there is optical spectral evidence for slower moving ejecta as well. By using the break frequencies of the radio spectrum as the nova shell transitioned from optically thick to optically thin, we estimated that the slowest ejecta had an expansion speed of v_i between 200 and 400 km s$^{-1}(d/6\mathrm{kpc})(T_b/10^4\mathrm{K})^{-1/2}$. The two components that were visible on day 832 had a separation of 70 mas on the plane of the sky, which, using a distance of 6 kpc, implies that each component had a velocity of roughly 440 km s^{-1} if they were ejected at $t = 0$ – consistent with our estimate for the innermost material. Additionally, Nagashima et al. (2013) modelled optical emission lines on days 7 and 11 with two overlapping Gaussian components with central velocities of -190 and 360 km s^{-1} relative to line of sight, also supporting a non-spherical distribution of ejecta with slow flows on the order of a few hundred km s^{-1}. Finally, the expected temperature behind a shock between two flows with velocities of 440 and 1500 km s^{-1} is $1.4 \times 10^7 \, (\frac{v_s}{1410\,\mathrm{km\,s^{-1}}})^2$ K (from equation 9), which is consistent with observational constraints on the temperature of the X-ray-emitting plasma (Krauss et al. 2011). That we measure a density profile close to $1/r^2$ from the transitioning ejecta indicates that the bipolar outflow likely had a wide opening angle. A model of V1723 Aql as a wide, biconical flow with collimating torus expanding at a few hundred km s^{-1} is consistent with imaging, optical and radio spectroscopy, the detection of X-ray emission, and the evolution of the radio light curve. The presence of more complex substructures or additional shocks could account for other variations in the radio light curve.

Fast biconical flows and slow equatorial tori may be more common than previously thought. For example, a change in the PA of maximum elongation like that in V959 Mon and V1723 Aql was also evident in Nova QU Vul, which had a double-peaked light curve much like that of V1723 Aql (Taylor et al. 1987, 1988). Early imaging of QU Vul showed bipolar structure, later evolving into a more spherical shape – suggesting that as the outer bipolar emission became optically thin, it revealed the central, more ring-like emission region (Taylor et al. 1987), as we saw in V1723 Aql.

That V1723 Aql displayed evidence for both shocks and dust production (Nagashima et al. 2013) around the time of the radio flare raises the intriguing possibility that dust production in novae is related to shocks. Both X-rays and radio synchrotron emission indicate that shocks were energetically important in V1723 Aql

roughly 40 ± 20 d into the eruption. Nagashima et al. (2013) argued based on optical observations that dust was produced around day 20. The finding by Metzger et al. (2014) that internal shocks generate a cool, dense post-shock region suggests that the appearance of shocks and dust at approximately the same time in V1723 Aql may be more than a coincidence.

5 CONCLUSIONS

Radio and optical imaging of novae has shown evidence for the formation of jets, e.g. RS Oph (Sokoloski et al. 2008); rings, e.g. DQ Her (Slavin et al. 1995; Sokoloski et al. 2013); clumping, e.g. T Pyx (Shara et al. 1997) and V458 Vul (Roy et al. 2012); collimating torus, e.g. V959 Mon (Chomiuk et al. 2014); and other asymmetries. For V1723 Aql, the contrast between the early- and the late-time radio emission reveals a system of colliding flows in the ejecta. This finding has broader implications for the production of γ-rays and the shaping of the ejecta from novae.

(i) Late-time radio emission from V1723 Aql was roughly consistent with a freely expanding thermal plasma with a well-defined inner edge, a temperature of 10^4 K, an ejecta mass of approximately 2×10^{-4} M$_\odot$, a ratio of minimum to maximum velocity $\zeta = v_i/v_{obs} \sim 0.2$, a maximum velocity of 1500 km s^{-1}, and a distance of 6 kpc.

(ii) The early-time radio flare was most likely due to a combination of thermal and non-thermal synchrotron emission emanating from the shocks that produced the observed X-ray emission. Thermal shocks alone fail to reproduce the high brightness temperature and weak X-ray emission.

(iii) The shocks that generated the early-time radio flare did not cause either the early optical light curve or the late-time radio evolution to significantly diverge from the expected behaviour of a standard fast nova. Relatively few novae have such comprehensive early-time radio observations, and thermal X-ray emission from shocks in novae is known to be common (Mukai et al. 2008) – therefore, detectable radio emission from early shocks could be more ubiquitous than previously realized.

(iv) It has been established that γ-ray production in the first few weeks of nova eruptions may be common (Ackermann et al. 2014; Metzger et al. 2015a). γ-rays are presumably the result of particle acceleration in shocks, early radio flares – as in V1723 Aql – may provide an important diagnostic of the shocks and colliding flows that produce γ-rays.

(v) Although the morpho-kinematic structure of the ejecta from V1723 Aql is not tightly constrained, its behaviour is consistent with that of a biconical flow loosely collimated by a slow equatorial torus, as in V959 Mon (Chomiuk et al. 2014). This hypothesis is supported by the existence of the perpendicular structures in the resolved radio images (see Fig. 3). Moreover, the shock speed derived from the difference between the fast radio flow (1500 km s^{-1}) and the slow radio flow (knots moving at $\sim$400 km s^{-1}) is consistent with that inferred from the temperature of the post-shock X-ray-emitting plasma. The flattening of the density profile seen from the variation in α_{trans} could be a consequence of the material being slightly more concentrated towards the equatorial plane in the inner region of the remnant (see Fig. 4).

Radio observations are a powerful diagnostic for the colliding flows and shocks that are crucial for γ-ray production and shaping of the ejecta from novae. The radio emission from V1723 Aql shows that the collision of fast and slow flows resulted in a shock which, although leaving the late-time behaviour of the radio light curve mostly unaffected, produced both thermal and non-thermal

emission. With the recent detections of classical novae in γ-rays, the question of relativistic particles in novae becomes even more important. Chomiuk et al. (2014) found the morphology of the shock-producing structures in V959 Mon; our work here extends those findings to other classical novae.

REFERENCES

Abbott D. C., Bieging J. H., Churchwell E., 1981, ApJ, 250, 645
Ackermann M. et al., 2014, Science, 345, 554
Balam D., Hsiao E. Y., Graham M., 2010, IAU Circ., 9168, 1
Barlow M. J., 1979, in Conti P. S., De Loore C. W. H., eds, Proc. IAU Symp. 83, Mass Loss and Evolution of O-Type Stars. Reidel, Dordrecht, p. 119
Bode M. F., Evans A., 2008, Classical Novae. Cambridge Univ. Press, Cambridge
Cao Y. et al., 2012, ApJ, 752, 133
Caprioli D., Spitkovsky A., 2014, ApJ, 794, 46
Cassinelli J. P., Hartmann L., 1977, ApJ, 212, 488
Chomiuk L. et al., 2012, ApJ, 761, 173
Chomiuk L. et al., 2014, Nature, 514, 339
Cunningham T., Wolf W. M., Bildsten L., 2015, ApJ, 803, 76
Della Valle M., Livio M., 1995, ApJ, 452, 704
Gaposchkin C. H. P., 1957, The Galactic Novae. North-Holland, Amsterdam
Heywood I., O'Brien T. J., Eyres S. P. S., Bode M. F., Davis R. J., 2005, MNRAS, 362, 469
Hjellming R. M., 1979, ApJ, 84, 1619
Hjellming R. M., 1996, in Taylor A. R., Paredes J. M., eds, Proc. ASP Conf. Ser. Vol. 93, Radio Emission from the Stars and the Sun. Astron. Soc. Pac., San Francisco, p. 174
Högbom J. A., 1974, A&AS, 15, 417
Kasliwal M. M., Cenko S. B., Kulkarni S. R., Ofek E. O., Quimby R., Rau A., 2011, ApJ, 735, 94
Kato T. N., 2015, ApJ, 802, 115
Krauss M. I. et al., 2011, ApJ, 739, L6
Lang K. R., 1980, Astrophysical Formulae. A Compendium for the Physicist and Astrophysicist. Springer-Verlag, Berlin (Heidelberg, New York)
Leitherer C., Robert C., 1991, ApJ, 377, 629
Metzger B. D., Hascoët R., Vurm I., Beloborodov A. M., Chomiuk L., Sokoloski J. L., Nelson T., 2014, MNRAS, 442, 713
Metzger B. D., Finzell T., Vurm I., Hascoët R., Beloborodov A. M., Chomiuk L., 2015a, MRNAS, 450, 2739
Metzger B. D., Caprioli D., Vurm I., Beloborodov A., Bartos I., Vlasov A., 2015b, preprint (arXiv:1510.07639)
Morlino G., Caprioli D., 2012, A&A, 538, A81
Mukai K., Orio M., della Valle M., 2008, ApJ, 677, 1248
Nagashima M. et al., 2013, in Di Stefano R., Orio M., Moe M., eds, Proc. IAU Symp. 281, Binary Paths to Type Ia Supernovae Explosions. Cambridge Univ. Press, Cambridge, p. 121
Nelson T. et al., 2014, ApJ, 785, 78
Park J., Caprioli D., Sptikovsky A., 2015, Phys. Rev. Lett., 114, 085003
Winkler, P. F.Ressler S. M., Katsuda S., Reynolds S. P., Long K. S., Petre R., Williams B. J., 2014, ApJ, 790, 85
Ribeiro V. et al., 2014, ApJ, 792, 57
Roy N., Kantharia N. G., Eyres S. P. S., Anupama G. C., Bode M. F., Prabhu T. P., O'Brien T. J., 2012, MNRAS, 427, L55
Rybicki G. B., Lightman A. P., 1979, Radiative Processes in Astrophysics. Wiley-Interscience, New York
Seaquist E. R., Palimaka J., 1977, ApJ, 217, 781
Seaquist E. R., Duric N., Israel F. P., Spoelstra T. A. T., Ulich B. L., Gregory P. C., 1980, AJ, 85, 283
Shafter A. W., 1997, ApJ, 487, 226
Shara M. M., Zurek D. R., Williams R. E., Prialnik D., Gilmozzi R., Moffat A. F. J., 1997, AJ, 114, 258
Slavin A. J., O'Brien T. J., Dunlop J. S., 1995, MNRAS, 276, 353
Sokoloski J. L., Rupen M. P., Mioduszewski A. J., 2008, ApJ, 685, L137
Sokoloski J. L., Crotts A. P. S., Lawrence S., Uthas H., 2013, ApJ, 770, L33
Staveley-Smith L., Briggs D. S., Rowe A. C. H., Manchester R. N., Reynolds J. E., Tzioumis A. K., Kesteven M. J., 1993, Nature, 366, 136
Taylor A. R., Pottasch S. R., Seaquist E. R., Hollis J. M., 1987, A&A, 183, 38
Taylor A. R., Hjellming R. M., Seaquist E. R., Gehrz R. D., 1988, Nature, 335, 235
Taylor A. R., Davis R. J., Porcas R. W., Bode M. F., 1989, MNRAS, 237, 81
Williams B. J. et al., 2014, ApJ, 790, 139
Wright A. E., Barlow M. J., 1975, MNRAS, 170, 41
Yamanaka M., Itoh R., Komatsu T., 2010, IAU Circ., 9167, 3

This paper has been typeset from a TeX/LaTeX file prepared by the author.